minerals

Article

Failure Behavior of Cuboid Granite Sample with a Circular Hole beneath a Bonding Fracture under Biaxial Compression

Diyuan Li, Jingtai Jiang and Feihong Gao *

School of Resources and Safety Engineering, Central South University, Changsha 410083, China
* Correspondence: feihong.gaoo@gmail.com

Abstract: Ore bodies incubating within fault zones are a common phenomenon in geological strata and pose a huge challenge for underground mining. To effectively exploit mineral resources, the layout of the mining roadway and the interaction between the roadway and geological fault must be considered. In this paper, a bonding fracture was formed on granite samples to simulate a closed fault, under which a circular hole was fabricated to simulate the roadway of the gold mine. We performed a biaxial compression test at a true-triaxial electrohydraulic servo testing system for granite samples with a combined fracture-hole structure. It is worth noting that the fracture inclination β and relative distance between fracture and hole L were taken into account. The digital image correlation (DIC) technique was used to observe the displacement and strain field evolution around the fracture-hole structure. Our results demonstrate that (1) the strength of the granite sample decreases with increasing bonding fracture dip angle β, and the displacement drops between the hanging wall and foot wall raised in both the horizontal and vertical displacement directions. Macroscopic cracks become dense, and the failure degree becomes severe around simulated fault areas. (2) With the increase in the distance L, the strength of the granite sample increases, the influence of the hole on the slip of the fracture plane is weakened, and the discontinuity of displacement becomes less obvious. (3) The maximum principal strain field quantitatively reveals the details of the crack initiation, propagation, and coalescence around the fracture-hole structure, and displacement nucleation is observed in the vertical displacement field.

Keywords: biaxial compression test; fracture-hole structure; crack propagation; strain evolution; digital image correlation

Citation: Li, D.; Jiang, J.; Gao, F. Failure Behavior of Cuboid Granite Sample with a Circular Hole beneath a Bonding Fracture under Biaxial Compression. *Minerals* **2022**, *12*, 1328. https://doi.org/10.3390/min12101328

Academic Editor: Giang Nguyen

Received: 23 August 2022
Accepted: 18 October 2022
Published: 20 October 2022

1. Introduction

During underground engineering, many collapse accidents occur in the process of roadway or tunnel excavation, which is generally caused by unreasonable construction and excavation schemes, or imperfect support measures around the fault zone [1–3]. Usually, accidents can be minimized by avoiding fault zones. However, when the ore body is to be mined in the fault area, it is inevitable to arrange roadways near the fault [4], as shown in Figure 1, Jiaojia Gold Mine is located in Laizhou City, Shandong Province, China. The actual geological characteristics are extremely complex, as abundant gold resources are detected underneath the fault zone, which poses a huge challenge for mineral resource extraction. To ensure the safe and efficient mining practice of Jiaojia gold mine resources and reduce roadway maintenance costs, it is necessary to pay attention to the interaction between geological faults and roadways [5]. Meanwhile, the intersection angle and relative distance [6,7] between roadways and faults are significant factors affecting roadway performance [8,9]. Hence, it is necessary to explore the influence of fault occurrence on roadway layout.

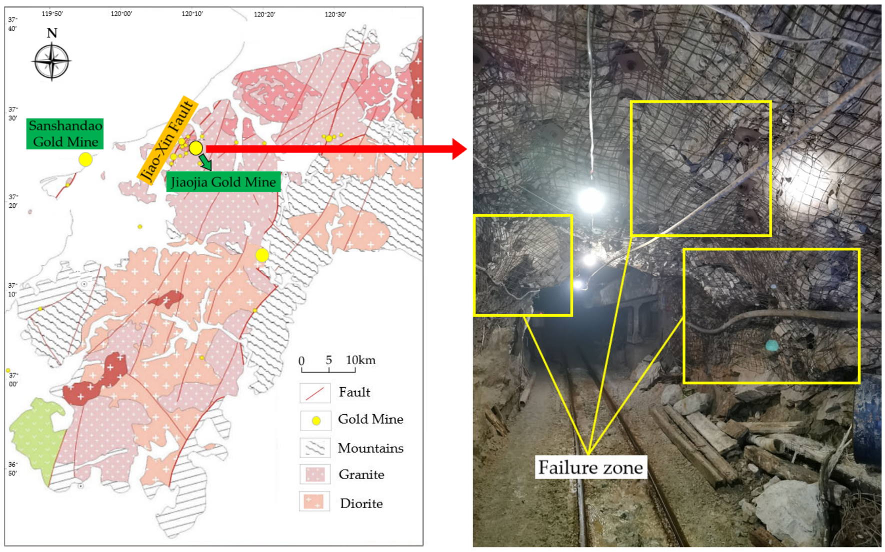

(**a**) (**b**)

Figure 1. Jiaojia Gold Mine in Jiaodong Peninsula. (**a**) Geological conditions of the Jiaojia Gold Mine; (**b**) failure zone of the roadway under the influence of the Jiao-Xin fault.

The surrounding rock stability and mechanical behavior of the roadway or tunnel construction have been widely studied. Some researchers carried out model tests to study the mechanical behavior of a circular tunnel with homogeneous strata [10,11] and analyzed the failure characteristics and strain field of the tunnel surrounding rock [12–16]. Precast cracks or faults have also been explored by a large volume of existing research [17–19]. However, due to the complex geological defects such as cracks and faults in the actual stratum, it is necessary to take these natural rock defects with roadways or tunnels into consideration to gain insight into their mutual effects. Among these existing studies, some studied the deformation characteristics and fracture evolution laws of fractured sandstone with prefabricated cavities [20,21]. Others used laboratory experiments and numerical analysis to study the failure characteristics of samples with combined defects of a single hole and oblique crack [8,21–23]. Many pieces of literature also studied the inclination of the fault and the distance between the fault and tunnel [24–28]. The existing research on the interaction between faults and roadways is limited to small-scale and numerical simulations. For field engineering practice, it is necessary to extend to carry out experimental research on large-scale structural planes.

Many researchers have conducted experiments on the impact of large-scale faults on tunnels or roadways based on engineering examples [2,12,29]. Some researchers have studied the influence of large faults on shallow tunnels and preventive measures [2,29,30], and carried out large-scale simulation tests to study the impact of faults on tunnels [12,31]. Some have used engineering examples and numerical simulations to study the impact of faults on mine shaft supports. Other studies have used numerical simulations to study the impact of faults on the stability of tunnels [9,32]. Although the above studies have considered the impact of large-scale structures on tunnels or roadways, which has certain practical engineering significance, experimental variables such as fault inclination and relative distance between fault and tunnel have not been considered, and have not been well explored in large-scale laboratory tests. To study the interaction between geological faults and roadways with varying fault occurrence, it is necessary to research the failure behavior of roadways beneath the simulated fault.

Therefore, we took the Jiaojia Gold Mine in Jiaodong Peninsula as the research background. As the lithology of the surrounding rock was mainly granite, granite was selected as the experimental material. The prefabricated hole and bonding fracture were used to simulate the fault and roadway. To better observe the deformation around the hole, a biaxial compression test was carried out, and the surface of the sample was observed by the DIC equipment. The failure behavior of roadways under a simulated fault was explored. The fracture behavior and evolution were studied accordingly, which guided engineering practice.

2. Methodology

2.1. Sample Preparation

The engineering background of this article is the Jiaojia Gold Mine in the Jiaodong Peninsula, which is used to determine the basic mechanical parameters of the granite. The uniaxial compression test was performed on cylindrical samples with dimensions of Φ 50 mm $\times$ 100 mm [33]. The basic mechanical parameters are listed in Table 1. Granite samples for formal tests were made with a height of 150 mm, a length of 150 mm, and a width of 40 mm. Before the test, the rock plate was cut in half with a high-pressure water jet method and then glued together with high-strength epoxy resin to simulate a closed fault. The strength of the epoxy resin herein was approximately 12 MPa. In addition, a circular hole was fabricated beneath the oblique fracture to simulate the roadway, as shown in Figure 2.

Table 1. Basic physical and mechanical parameters of the granite sample.

Properties	Value
Young modulus E_s (GPa)	47.01
Poisson ratio ν	0.28
Uniaxial compressive strength σ_c (MPa)	125.87
Uniaxial tensile strength (MPa)	6.7
Longitudinal wave velocity V_p (m/s)	3692.9
Density ρ (kg/m^3)	2666.7

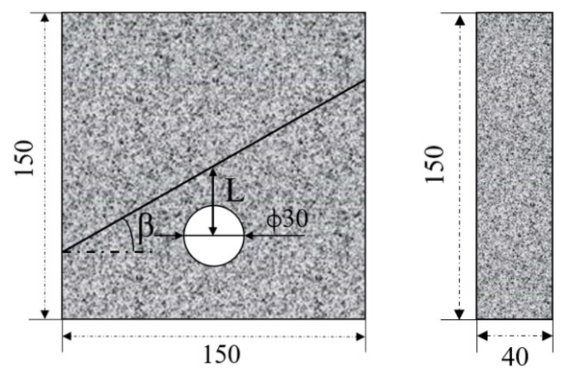

Figure 2. Schematic diagram of the granite sample in the biaxial compression test.

The purpose of this test is to study the influence of the fault dip angle and the distance between the roadway and the fault on the induced instability and failure of the surrounding rock by changing the variables β and L (as shown in Figure 1). Therefore, the samples can be divided into the following groups (as shown in Table 2):

(1) A-0, A-15, A-30, and A-45 are granite samples with fault dip angles of 0°, 15°, 30°, and 45°, and the distance L between the hole center and the fault is 40 mm.

(2) L-1, L-2, and L-3 are granite samples with distances L between the hole center and the fault of 30 mm, 35 mm, and 40 mm, respectively, and the fault dip angle is 30°. Considering the effect of the size effect, the hole bottom should not be too close to the sample boundary.

(3) C is the control group. The sample only contained a central hole without a prefabricated fault.

(4) O is the control group, the fault was not bonded with glue, and the fault dip angle was 30°. Considering that the stress propagation of the unbonded fault might be

blocked, the minimum distance L between the hole and the fault was 30 mm. The details regarding different types of samples are listed in Table 2.

Table 2. Morphology and mechanical parameters of granite samples.

Sample No.	Length/mm	Width/mm	Thickness/mm	Hole	Bonding Fracture	Angle	Distance between Fracture and Hole/mm
A-0	151.95	149.96	41.03	√	√	0°	40
A-15	149.45	149.66	40.56	√	√	15°	40
A-30	150.36	151.30	40.35	√	√	30°	40
A-45	153.12	152.22	41.02	√	√	45°	40
L-1	152.23	151.28	42.34	√	√	30°	30
L-2	149.36	150.34	39.86	√	√	30°	35
L-3	151.42	152.03	40.16	√	√	30°	40
C	151.42	151.30	41.12	√	-	-	-
O	150.35	152.21	42.01	√	×	30°	40

Moreover, the DIC technique was used to record the evolution process of the strain field and displacement field on the surface of the granite sample. Before the test begins, artificial speckle patterns should be printed on the surface of the sample to facilitate analysis and processing. Meanwhile, the low-speed camera of the CMOS sensor was placed 60 cm in front of the samples. The lamp was placed obliquely above the sample to supplement the illumination (as shown in Figure 3).

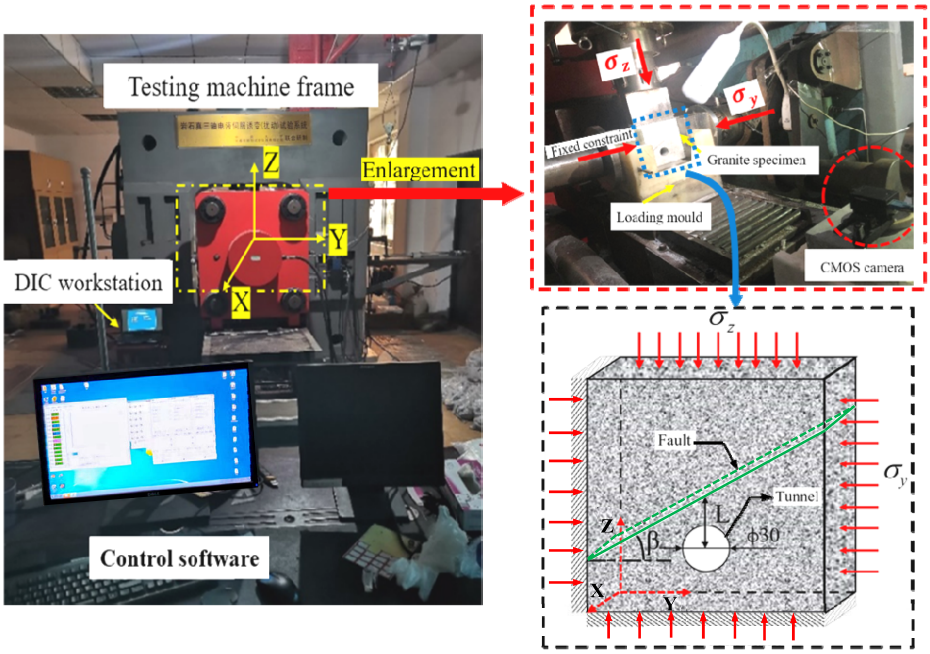

Figure 3. True-triaxial testing equipment and schematic diagram of the loading method for the sample.

The resolution of the camera is 4096 × 3000 pixels, with 8-bit gray digitalization. The camera automatically captures images at a frame rate of 10 frames per second. After filming, speckle images captured were analyzed using VIC-2D software. More details about the DIC technique and artificial speckle pattern can be found in the references [17,34,35]. The instrument used in this experiment is true triaxial equipment, which can realize loading stresses in one direction, two directions, and true-triaxial conditions. It can control the load, deformation, and displacement automatically. The experimental system is a digital closed-loop control system composed of a computer, control software, testing machine frames, and sensing element, as shown in Figure 3. The test device can apply a maximum force of 2000 kN in the X-axis and Y-axis directions and 3000 kN in the Z-axis direction [36–39].

2.2. Experimental Procedure

2.2.1. Determination of In Situ Stress

The three principal stresses at the depth of the Jiaojia Gold Mine are as follows: the maximum horizontal principal stress was up to 51.1 MPa (306.6 kN) and the vertical in-situ stress reached 27 MPa (162 kN). The details of the initial stresses are listed in Table 3. Loading to the initial set value at a loading rate of 1 kN/s was in the directions σ_y and σ_z [40].

Table 3. Initial in situ stress at the depth of the Jiaojia Gold Mine.

Depth (m)	σ_z (MPa)	σ_{ymax} (MPa)	σ_{ymin} (MPa)
1000	27	51.1	33.7

2.2.2. Loading Paths

To reduce the friction effect, petroleum jelly was smeared on four contact surfaces of sample boundaries. Four clamps were placed between the sample and loading end regions of the equipment to fix the granite sample, and one end region was fixed; the other end region was the loading face. After placing the sample and adjusting the test equipment, a preload of 2 kN was applied. When the preload reached 2 kN, the loading rate was fixed at 1 kN/s to a setting value [41].

The loading path is shown in Figure 4, and the specific loading procedure is described as follows:

(1) The σ_y and σ_z directions were loaded to 162 kN at a loading rate of 1 kN/s. The σ_z direction remained constant, and σ_y continued to be loaded to 306.6 kN.

(2) After the preset in situ stress was reached, σ_z maintained the stress level, and σ_y carried out graded loading at a rate of 1 kN/s. When the stress reached 306.6 kN, the stress was maintained for 2 min for every 60 kN increase. The purpose was to prevent the sample from suddenly failing.

(3) There was obvious damage and severe damage to the hole wall, the load was removed, the load of σ_y was first unloaded to σ_z, and then σ_y and σ_z were unloaded to 0.

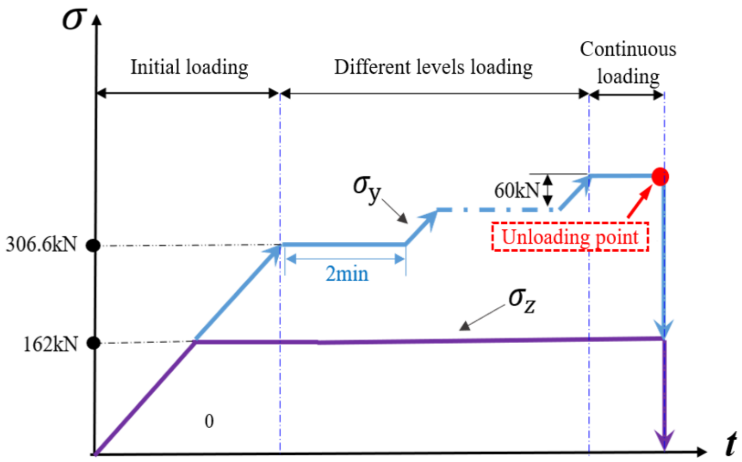

Figure 4. Schematic diagram of the loading path.

3. Results

3.1. Mechanical Properties

Biaxial compressive strength reflects the resistance of samples with bonding fracture, and it was represented by the peak strength of σ_y in this study. Take sample *L*-2 as an example. σ_y and σ_z reached the set vertical in situ stress (162.6 kN) with the same loading rate first. σ_z maintained stability, while σ_y maintained the original loading rate. Once the sample was damaged, σ_{ymax} (421.9 kN) was specified as the biaxial compressive strength. The biaxial strength of granite samples with different geometric fracture patterns is summarized in Table 4.

Table 4. Mechanical parameters of different types of rock samples.

Initial Stress	A-0	A-15	A-30	A-45	L-1	L-2	L-3	C	O
σ_z/MPa	27.03	28.07	27.08	28.27	28.32	28.46	27.70	27.92	28.60
σ_y/MPa	91.24	85.17	69.76	53.08	62.72	70.32	77.69	84.09	92.90

Furthermore, Figure 5 shows the relationship between the biaxial compressive strength versus fracture dip angle (Figure 5a) and spacing distance *L* (Figure 5b). When the dip angles of the fracture were 0°, 15°, 30°, and 45°, the biaxial compressive strength of the rock sample was 91.24 MPa, 85.17 MPa, 69.76 MPa, and 53.08 MPa, respectively, which demonstrated a decreasing trend. In addition, when the relative distance between the hole and the fracture was 30 mm, 35 mm, and 40 mm, the biaxial compressive strength was 62.72 MPa, 70.32 MPa, and 77.69 MPa, respectively. The results demonstrated that with increasing distance *L*, the interaction between the fracture and the hole was weakened, and the strength of the rock sample increased.

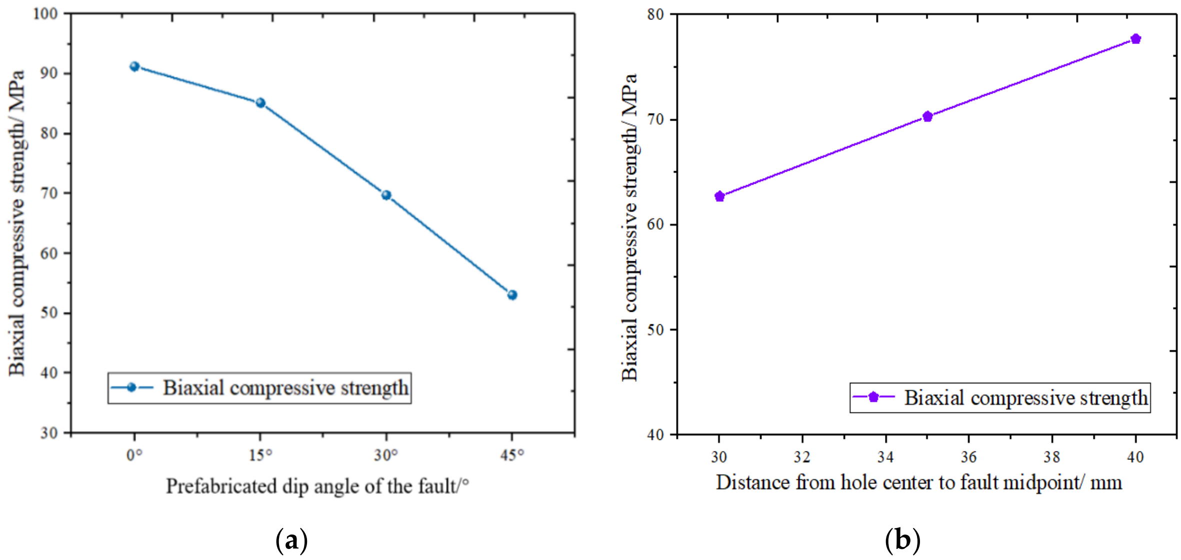

Figure 5. Biaxial compressive strength of different types of samples. (**a**) Fault dip angles-Biaxial compressive strength curve; (**b**) Distance from fault to hole center -Biaxial compressive strength curve.

3.2. Failure Mode

To obtain an accurate and intuitive fracturing pattern on the sample surface, all the experimental pictures collected during the test were further processed by the VIC software. The deformation on the sample surface is outlined by black lines (as shown in Figures 6 and 7). Dense areas of fine lines in the image indicate the microscopic deformation concentrated area, whereas the bold lined areas indicate macroscopic cracks.

Figure 6 shows the images of the final crack transfixion mode of different types of samples. Figure 6a,b show sample C with a hole and sample O with an unbonded fracture, respectively. The generating crack amount in these two types was small and mainly distributed at the footwall, indicating that the stress concentration generally occurred below the hole. In addition, there were no visible cracks around the unbonded fracture plane, indicating that the influence of the hole on the unbonded fracture plane was negligible.

The failure modes of granite samples with bonded fracture dip angles of 0°, 15°, 30°, and 45° are shown in Figure 6c–f. When the fracture dip angle was 0°, newborn cracks formed around the fracture plane end, and there were no obvious macrocracks generated around the fracture-hole structure, indicating that the fracture plane of 0° had a relatively weak effect on the fracture-hole zone, which also helped verify the conclusion that the A-0 type had the largest strength. When the fracture dip angle was 15°, a macroscopic crack initiated from the middle of the fracture plane and extended to the hanging wall. At the same time, the roof and floor of the hole fractured and formed a V-shaped groove. When the fracture dip angle was 30°, the dominant crack was formed above the fracture plane and spread to the upper left direction. Several macroscopic cracks generated at the top of the hole extended continuously and tended to connect with the main crack on the other side of the fracture plane. When the crack was 45°, numerous macroscopic cracks were derived from the fracture plane toward the hanging wall. Among them, the dominant crack expanded from the middle of the fracture plane, and many secondary cracks were generated beside the main crack. A small number of cracks can be observed in the footwall and extend horizontally. Cracks were formed at the top of the hole and extended horizontally to the right.

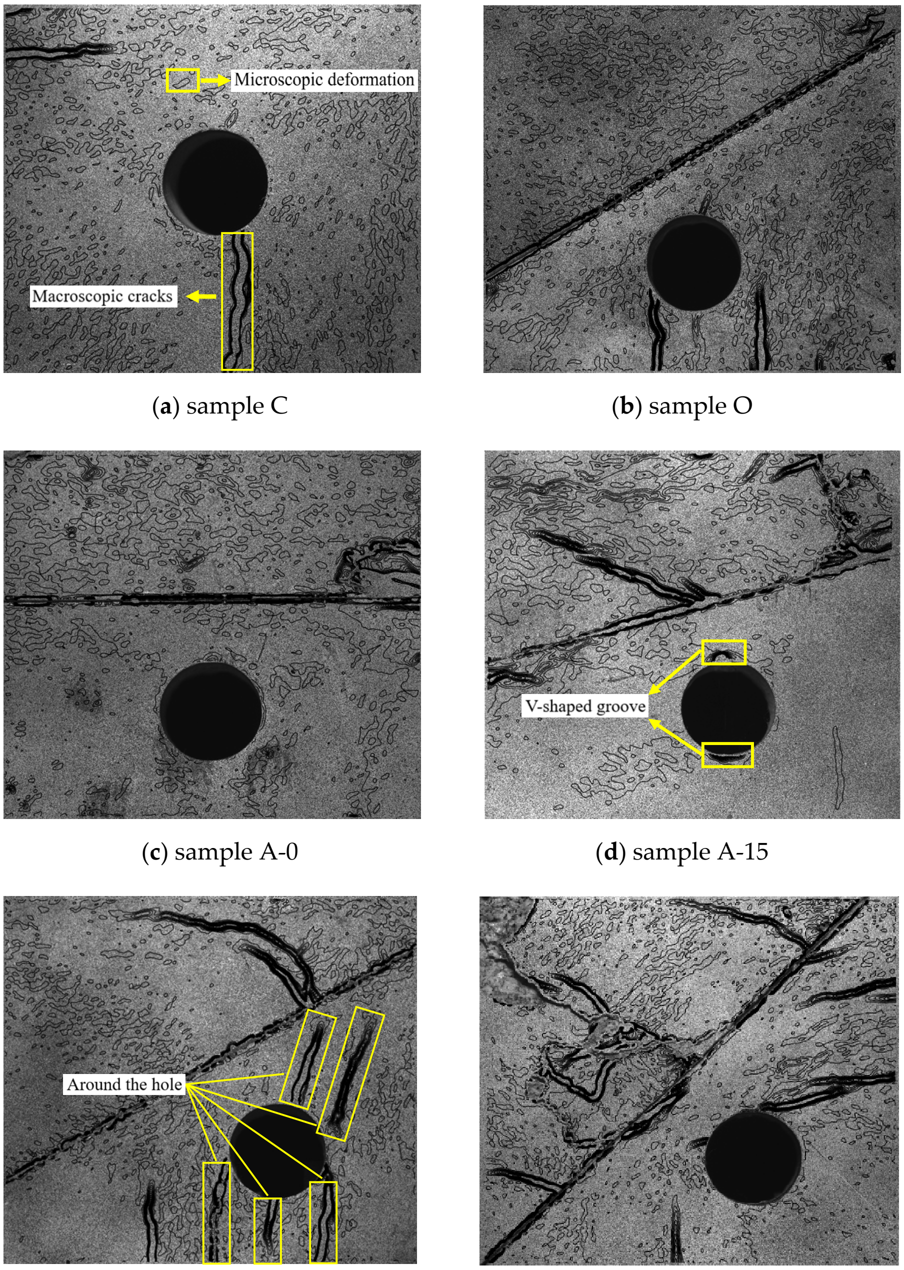

(**a**) sample C (**b**) sample O

(**c**) sample A-0 (**d**) sample A-15

(**e**) sample A-30 (**f**) sample A-45

Figure 6. Fracture modes of granite samples with different bonding fracture dip angles.

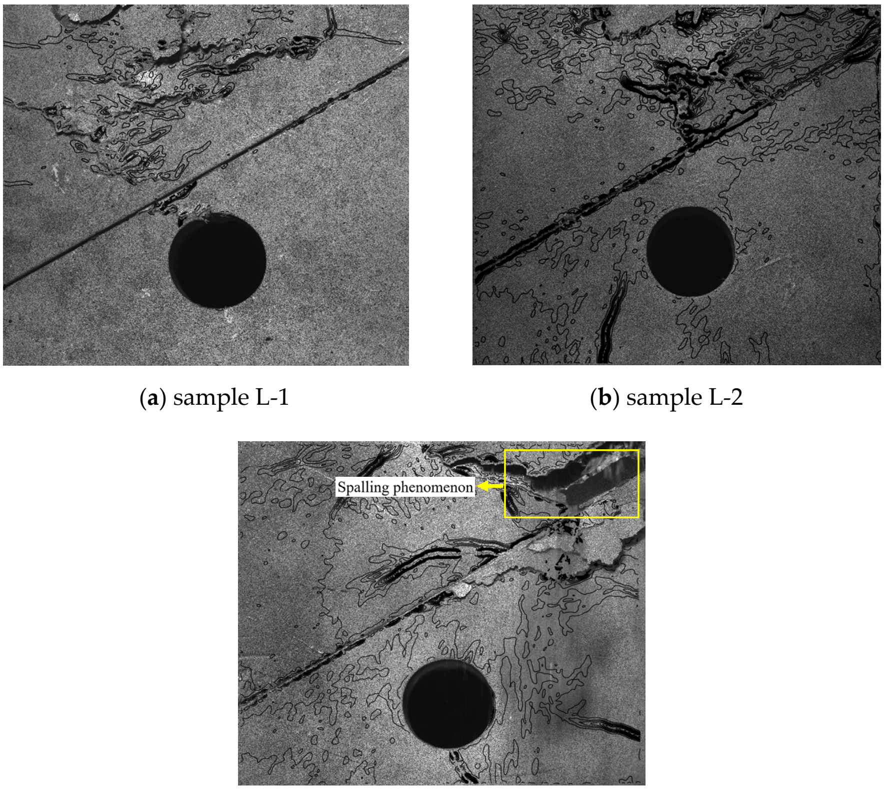

(**a**) sample L-1 (**b**) sample L-2

(**c**) sample L-3

Figure 7. Fracture modes of granite samples with bonding fracture at different spacing distances *L*.

The failure modes of rock samples with a spacing distance *L* ranging from 30 mm, 35 mm to 40 mm are shown in Figure 7a–c. It can be observed from Figure 7 that when the spacing distance was 30 mm, there were small-scale cracks between the hole and fracture plane, and they crossed the fracture plane. Finally, a divergent failure zone appeared on the hanging wall. When the spacing distance *L* was 35 mm, some cracks initiated from the fracture plane, and these cracks mainly gathered on only the hanging wall and extended to the boundary. Finally, the expansion and connection of macroscopic cracks led to the overall failure. When the distance between the hole and the fracture plane was 40 mm, cracks formed at the right end regions of the fracture zone while fracturing below the fracture plane. A crack was also formed under the hole and extended down to the bottom boundary of the sample.

In conclusion, when the spacing distance *L* is closed, the hole has a great influence on the fracture plane, and newborn cracks accumulate mainly in the middle region between the fracture and hole and further diffuse upward across the fracture plane. When the spacing distance *L* is far (*L* = 35 mm, 40 mm), the interaction between the fracture and hole is limited, and dominant macrocracks form in the hanging wall rather than dense microcracks.

4. Discussion

4.1. Discontinuity Analysis of Displacement

4.1.1. Fracture Slip Behavior

Static loads were applied in the Y and Z directions, and an LS camera was placed along the X direction to monitor the fracturing process. As shown in Figure 8 (A-0 and A-30 for examples), one platen was fixed, and the other end was subjected to axial static pressure. Figure 8a shows that when the fracture dip angle was 0°, the loading platen transmitted force to the granite sample from the upper and lower contact areas. Under such conditions, the contact area remained the same for the upper and lower parts, but the hole that existed in the lower part resulted in different stress distributions. Two mass points along the fracture plane were analyzed. The displacement of two mass points could be decomposed into the slip distance along the fracture plane and vertical displacement resulting from the decomposed normal force. For the cases of fracture dip angles not equal to 0° (Figure 8b), the contact area of the upper part could be larger than that of the lower part, and the stress in the footwall, therefore, could be greater than that of the hanging wall. Furthermore, the footwall contained a hole, which further intensified the stress concentration around the hole. The asymmetry of the stress distribution led to the displacement difference along the fracture plane.

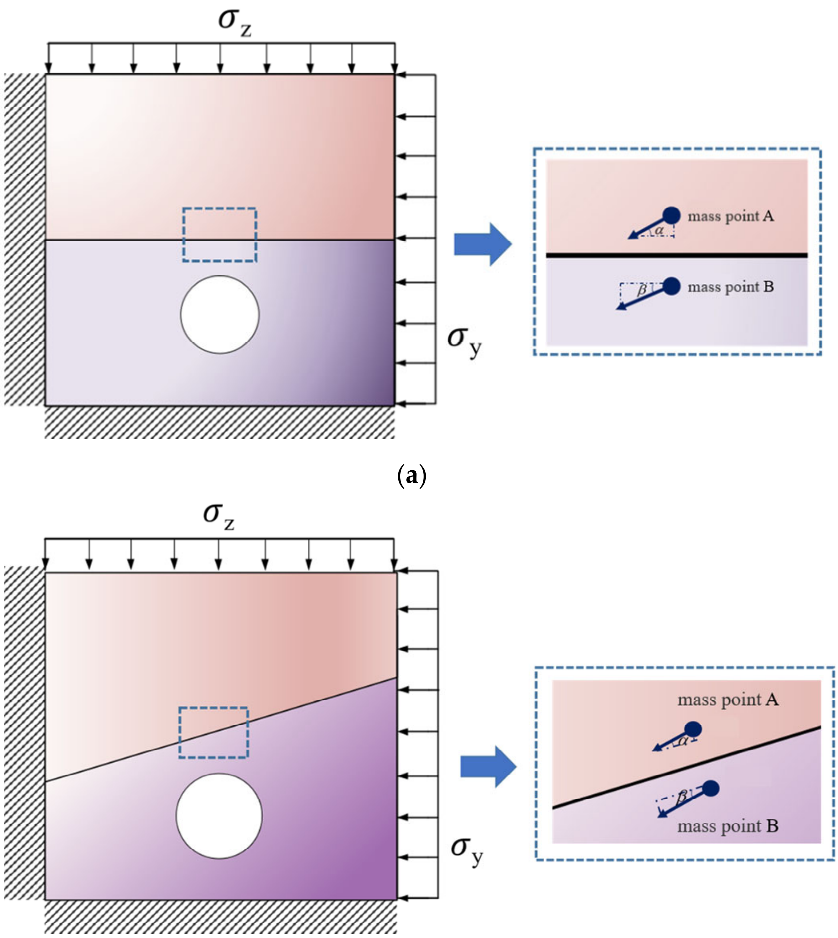

(**a**)

(**b**)

Figure 8. Loading mode diagram and sliding along the fracture plane for granite samples: (**a**) A-0; (**b**) A-30.

Furthermore, the displacement field on the sample surface can explain the failure mechanism. Taking the A-0 sample as an example, the displacement vector diagram was drawn using speckle data from VIC-2D software, as shown in Figure 9. This result indicated that the displacement vectors of the sample all inclined downward, which was related to the loading mode specified in Figure 8. This section analyzes the fracture slip value for different types of samples. The method to measure fracture slip is elaborated as follows:

(1) Determining the position of measurement points: points A and C were 2 cm away from the left and right boundaries, respectively, and point B was located directly above the hole.
(2) To analyze the fracture slip value of measurement points A, B, and C, reference points for each measurement point were taken above and below the fracture plane, as shown in Figure 9 (A_1, A_2, B_1, B_2, C_1, C_2). According to the displacement decomposition

method shown in Figure 8, the slip value along the fracture plane was derived for points A, B, and C.

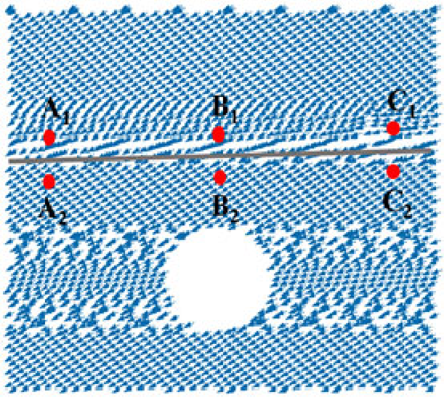

Figure 9. Displacement vector diagram of granite sample A-0 (σ_y = 90% σ_{ymax}).

After specifying the calculation method, the curves of the slip values for positions A, B and C are shown in Figures 10 and 11. Negative values on the plots indicate a downward slip along the fracture plane.

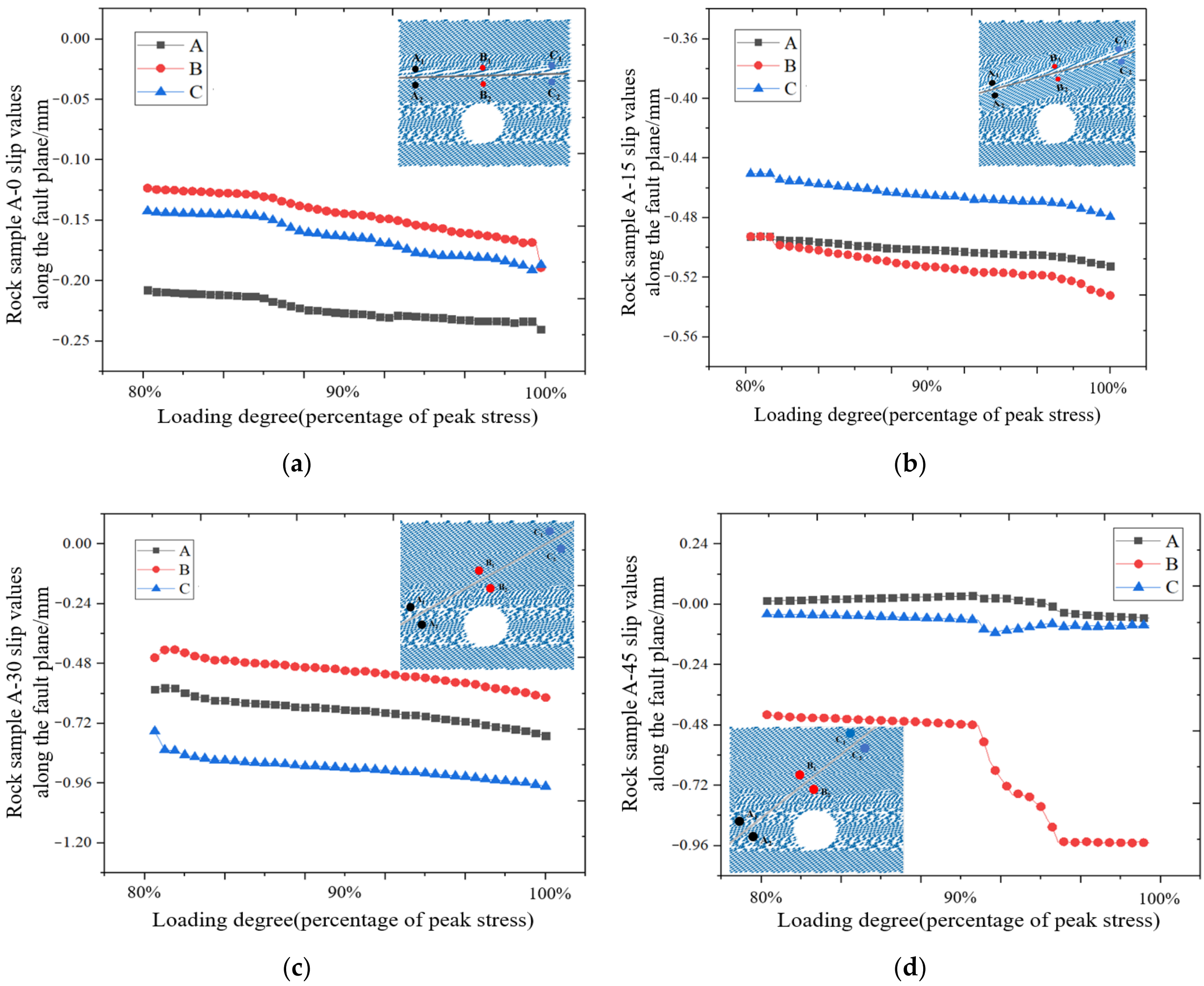

Figure 10. Schematic diagram of the relationship between fracture slip at measurement points and loading degree in group A. (**a**) sample A-0 slip values; (**b**) sample A-15 slip values; (**c**) sample A-30 slip values; (**d**) sample A-45 slip values.

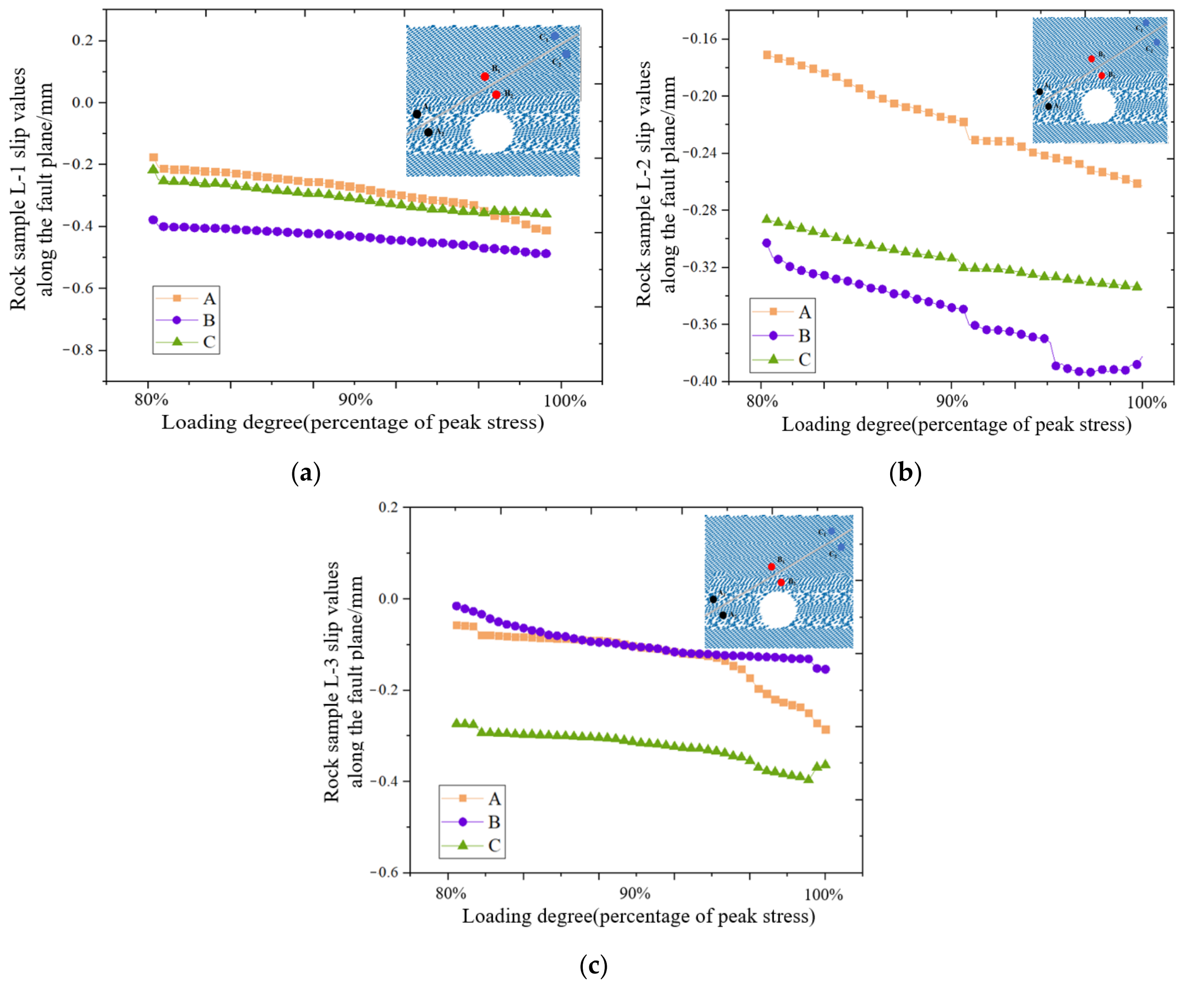

Figure 11. Schematic diagram of the relationship between fracture slip at points A, B, C, and loading degree in group *L*. (**a**) sample L-1 slip values; (**b**) sample L-2 slip values; (**c**) sample L-3 slip values; (**a**) sample A-45 slip values.

From Figures 10 and 11, it was concluded that for the A-0, A-15, and A-30 types, the slip values of the same locations (A, B, and C) generally increased with the increasing fracture dip angle (except for the measurement point B in Figure 10b-c, which were quite close). The behavior of sample A-45 was inconsistent with that of the other types of samples. The slip value of point B above the hole was significantly higher than that of points A and C, which were quite small and close to 0.

Figure 11 shows the relationship between slip values along the fracture plane and loading degree. The main characteristics were summarized as follows:

(1) When the fracture plane was close to the hole, the slip value at point B was the largest, followed by point C, and the slip value at point A away from the loading platen was the smallest. The slip values at points A and C of sample *L*-1 were similar, and the slip value at point B above the hole was larger, reaching 0.48 mm at peak stress. The slip value of point A at the left boundary of sample *L*-2 was the smallest, followed by point C at the right end, and the slip value for point B was the largest (less than *L*-1).

(2) When the fracture was far from the hole, the influence of the hole on fracture slip was reduced, the slip value of point B above the hole and point A away from the loading platen were small and similar, and point A increased obviously when the peak strength was reached. The slip value of position C near the loading platen was the largest.

4.1.2. Displacement Discontinuity

In the test process, fracture-dislocation occurred, and discontinuous displacement occurred on both sides of the fracture. To study the discontinuity of displacement on both sides of the fracture plane, a monitoring belt was arranged in the direction of the vertical fracture plane. The vertical fracture plane monitoring zone was arranged in the center of the opposite hole and perpendicular to both sides of the fracture plane, with a length of 10 mm.

Taking the sample A-0 as an example, the calculation method of the discontinuity of fracture displacement was elaborated. To analyze the displacement drops along the fracture at peak strength, the load-time curve of the granite sample A-0 was drawn in Figure 12 first, and then the displacement in the middle period of 950 s~1088 s was taken for analysis.

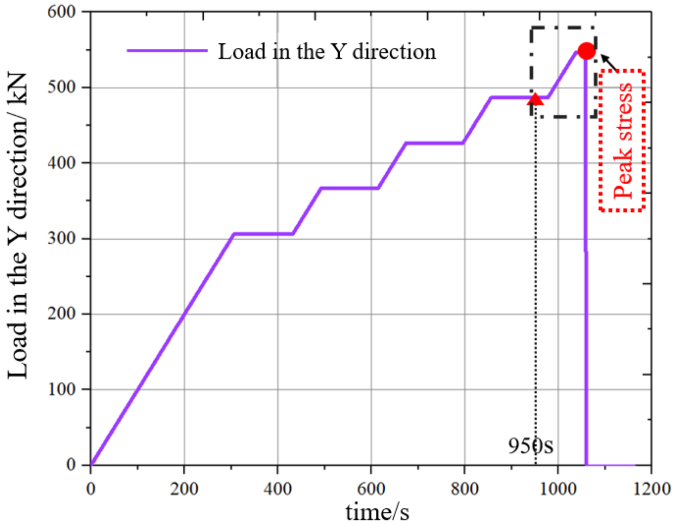

Figure 12. Load-time curve of sample A-0.

First, the horizontal and vertical displacement drops of the monitoring belt at different times are shown in Figures 13 and 14, respectively. In Figure 13a, the horizontal displacement line from M to N is depicted. The line breaking in the middle indicated the discontinuity of displacement for a certain time. Then, a series of horizontal displacement lines at a time range of 950 s~1088 s was deduced and drawn in Figures 13 and 14.

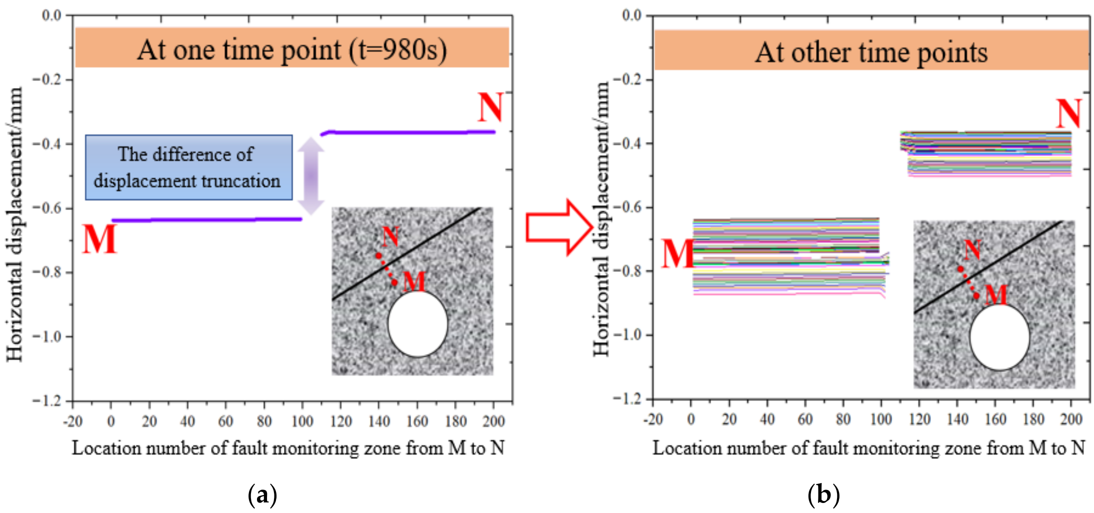

Figure 13. The horizontal displacement drops of granite sample A-0 during 950 s~1088 s. (**a**) The horizontal displacement drops when t=980 s; (**b**) The horizontal displacement drops when other time points.

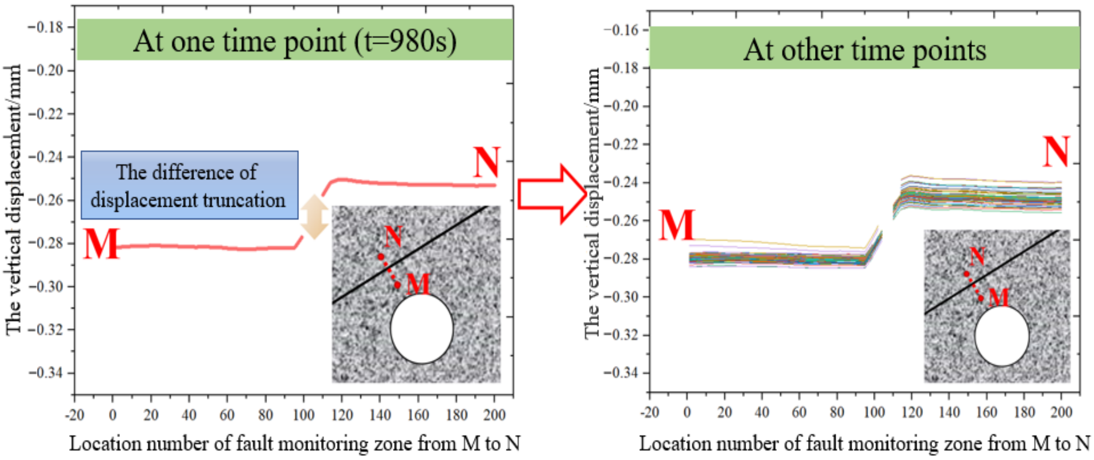

(**a**) (**b**)

Figure 14. The vertical displacement drops of granite sample A-0 during 950 s~1088 s. (**a**) The vertical displacement drops when t=980 s; (**b**) The vertical displacement drops when other time points.

Second, calculate the displacement drops for every time point. Each displacement line is shown in Figures 13b and 14b. The scatter diagram of the drop values versus time range in 950 s~1088 s was plotted (as shown in Figure 15a,b). Figure 15a shows that the discontinuity of horizontal displacement slowly rises with time. In Figure 15b, an obvious linear relationship was not shown, but the displacement drops were maintained at 0.022–0.025 mm before the sample reached failure. To ensure accuracy, the mean value of the scattered points within this range was taken as the vertical displacement discontinuity value for sample A-0, as shown in Figure 15b.

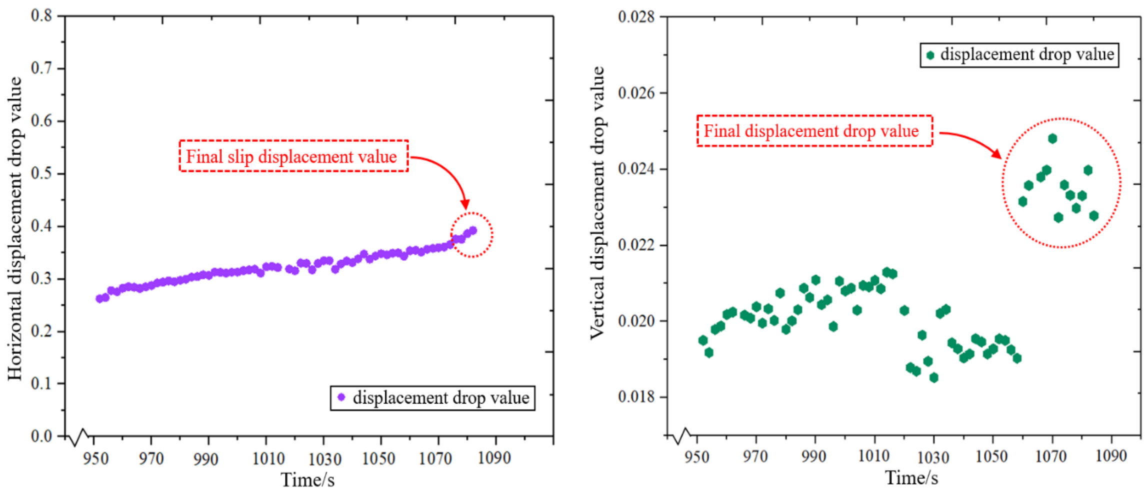

(**a**) (**b**)

Figure 15. Final displacement drops value. (**a**) Final vertical drops in the horizontal direction in 950 s~1088 s (**b**). Final vertical drops in the horizontal direction in 950 s~1088 s.

Finally, the displacement drop value of the granite sample was calculated and compared. The relationship between the horizontal and vertical displacements dropped and different angles were obtained and are shown in Figure 16. As shown in Figure 16a, with increasing fracture dip angle, the displacement drops increased as well. The horizontal displacement drop value of the unbonded fracture (sample O) was 0.221 mm, while the horizontal displacement drop values of the 0°, 15°, 30°, and 45° bonded fractures were 0.393 mm, 0.554 mm, 1.282 mm, and 1.344 mm, respectively. According to Figure 16b, the vertical displacement drop value of the unbonded fracture was 0.051 mm, while the displacement drop values of the 0°, 15°, 30°, and 45° bonded fractures were 0.024 mm, 0.248 mm, 0.594 mm, and 0.611 mm, respectively. Except for the unbonded fracture type O, the vertical displacement drop value generally demonstrated a rising trend with increasing angle. However, compared with the horizontal displacement, the drop value of the vertical displacement was reduced by half. This may be caused by the vertical direction Z being loaded to 162 kN and remaining at this level, but the Y-axis loading continues until the sample reaches failure, so the displacement drop in the horizontal direction is significantly greater than that in the vertical direction. Furthermore, Figure 16b shows that the vertical displacement drop of sample O is between sample 0° and sample 15°, mainly because the fracture dip angle of control group O was 30°, and the influence of the vertical load on the fracture displacement drops was lower than that of the fracture dip angle (30°).

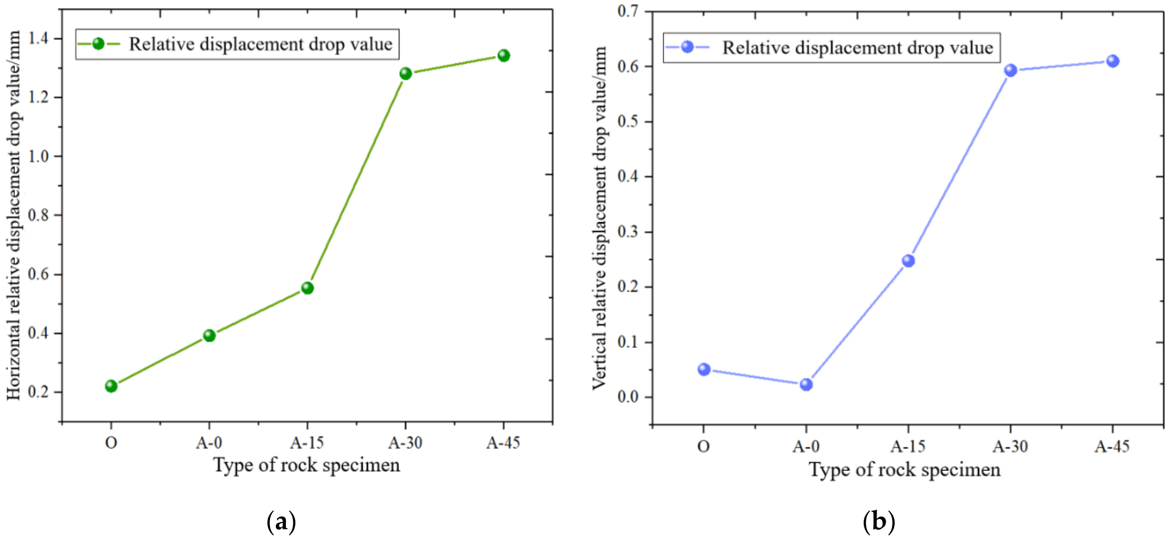

Figure 16. The displacement truncation difference of different types of rock samples of group A; (**a**) Horizontal displacement; (**b**)Vertical displacement.

Figure 17 shows the displacement drop of different types in group *L*. The closer the distance between the fracture and the hole was, the more obvious the discontinuity of the displacement was, except for the unbonded type O (displacement drops value was 0.221 mm). The horizontal displacement drop values of the samples with spacing distances of 30 mm, 35 mm, and 40 mm were 0.555 mm, 0.265 mm, and 0.234 mm, respectively. The drop value characteristics for vertical displacement were similar to those of group A, with nearly half reduction for horizontal displacement. The drop values of the vertical displacement were 0.238 mm, 0.167 mm, and 0.150 mm, respectively. The distance between the fracture and hole was close, and the discontinuity of horizontal and vertical displacement was significantly greater than that of other granite types.

4.2. Evolution of the Deformation Field

4.2.1. Evolution of the Major Principal Strain Field

To analyze the major principal strain field on the sample surface under biaxial compression, several typical samples in groups A, *L*, and O were selected to discuss the evolution of fracturing for different sample types.

The evolution process of the major principal strain field of sample A-15 is shown in Figure 18. According to Figure 18, when the load reached 84.7% of the peak strength, strain concentration did not occur around the hole, only a slender crack appeared at the bottom boundary of the sample, and stress concentration occurred on the fracture plane. When the load reached 92.32% of the peak strength, there was no high strain around the hole, but strain began to concentrate at the left fracture end. While the load reached 98.39% of the peak strength, a high-strain concentration formed at both the roof and floor of the hole, and a large-scale high-strain concentration also appeared in the hanging wall. When the strength peak was reached, regional failure occurred on the hanging wall, and the surface flaked.

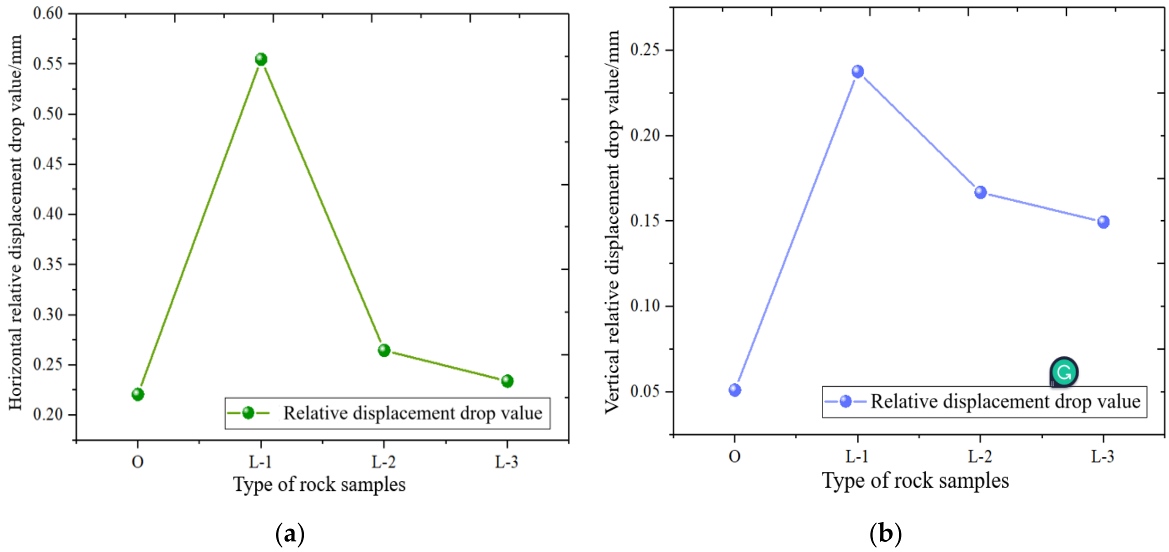

Figure 17. The displacement drops of different types of granite samples in group *L*. (**a**) The Horizontal displacement of samples; (**b**) The vertical displacement of samples.

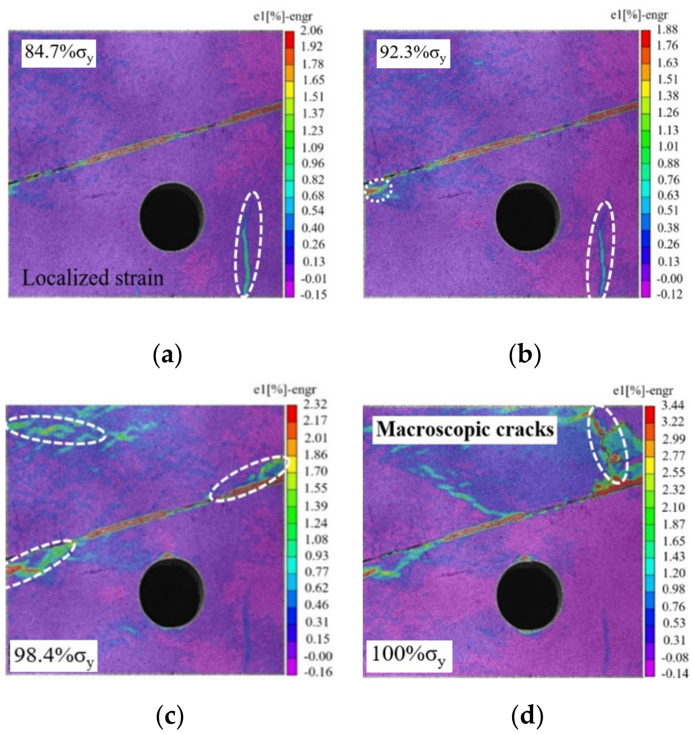

Figure 18. Evolution process of the major principal strain field of sample A-15. (**a**) 84.7%σ_y; (**b**) 92.3%σ_y; (**c**) 98.4%σ_y; (**d**) 100%σ_y.

The evolution process of the major principal strain field of sample A-30 is shown in Figure 19. When the load reached 84.2% of the peak strength, a high-strain concentration appeared in the lower left area of the footwall. A high-strain band initiated from the hole floor, which expanded along the loading direction. When the load reached 85.2% of the peak strength, the original high-strain zone expanded further. When the load reached 90.4% of the peak strength, the high-strain zone at the hole floor extended to the left boundary, and the strain zone appeared at the hole crown and tended to connect with the fracture plane. When the sample reached its peak strength, the strain concentrated at the top and bottom of the hole, forming a V-shaped groove. The crack initiated from the hole crown and connected with the cracks formed at the left end of the fracture plane.

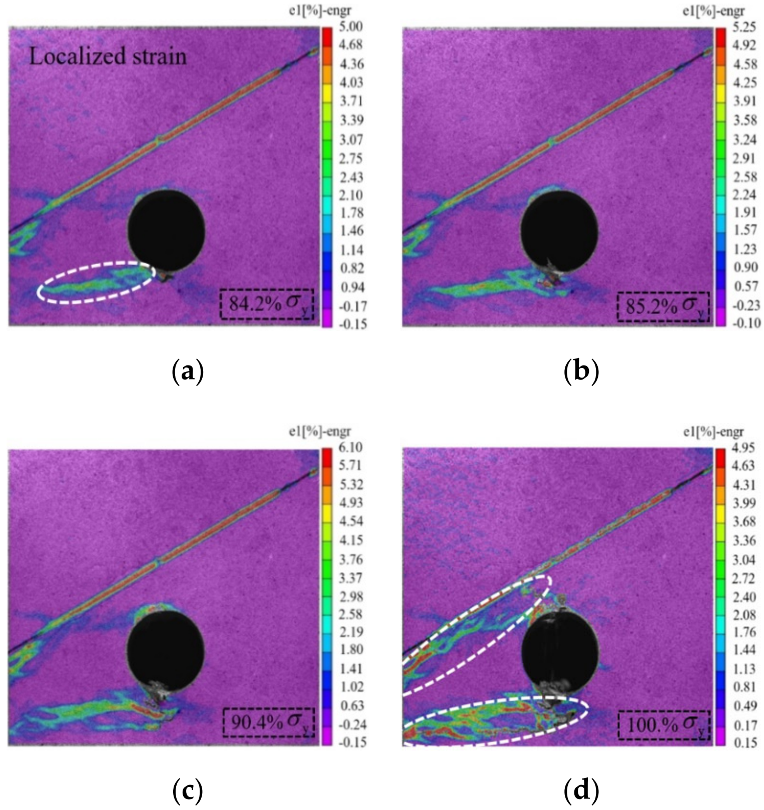

Figure 19. Evolution of the major principal strain field of sample A-30. (**a**) 84.2%σ_y; (**b**) 85.2%σ_y; (**c**) 90.4%σ_y; (**d**) 100%σ_y.

The evolution process of the major principal strain field of sample *L*-2 is shown in Figure 20. When the load reached 87.4% of the peak strength, little high strain appeared on both the top and bottom of the hole, and a crack initiated from the fracture plane and extended to the hanging wall. When the load reached 92.2% of the peak strength, the original high-strain zone around the hole expanded further, and a new crack was formed at the sample boundary and extended to the hole floor. Scattered high-strain zones are concentrated at the lower right end of the fracture plane. When the load reached 96.5% of the peak strength, the original crack extended further, and a new crack was generated at the bottom boundary of the sample. Meanwhile, a stress concentration area appeared at the upper right of the fracture plane. When the sample reached the peak strength, regional failure appeared on the upper right of the fracture plane, and a crack directly penetrated the fracture.

Figure 21 shows the evolution process of the major principal strain field of sample *L*-3. Figure 21 shows that when the load reached 87.7% of the peak strength, an obvious high-stress concentration occurred in the fracture plane, and small-scale high strain appeared above the hole. When the load reached 91.0% of the peak strength, ejection occurred at the hole floor, and a weak surface tangent to the hole crown appeared, which almost penetrated through the whole sample. When the load reached 95.7% of the strength, new cracks were generated from the hole floor and extended to the left boundary of the sample. When the load reached its peak strength, regional failure and cracks appeared in the right part of the hanging wall. The spalling phenomenon could be observed on the hole floor, accompanied by tensile cracks. The hole top and fracture surface formed a wedge block.

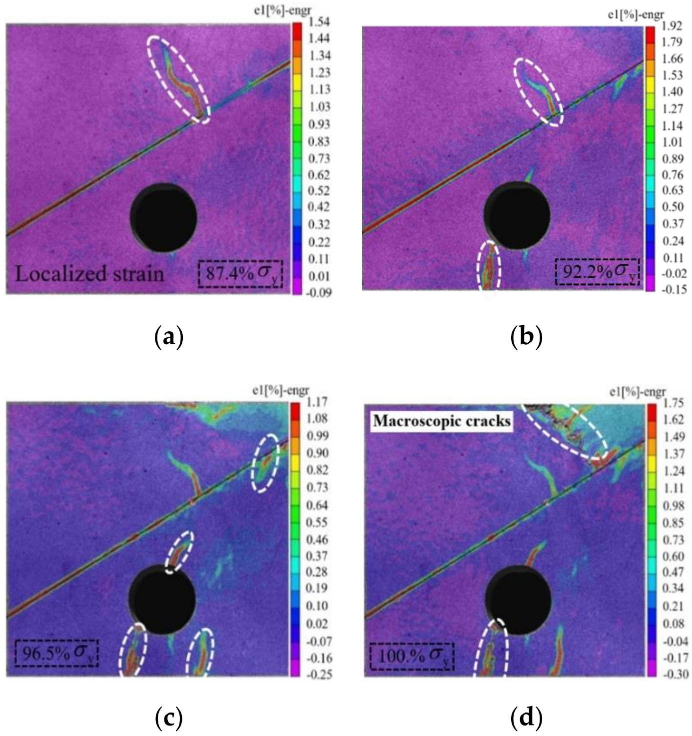

Figure 20. Evolution process of the major principal strain field of sample *L*-2. (**a**) 87.4%σ_y; (**b**) 92.2%σ_y; (**c**) 96.5%σ_y; (**d**) 100%σ_y.

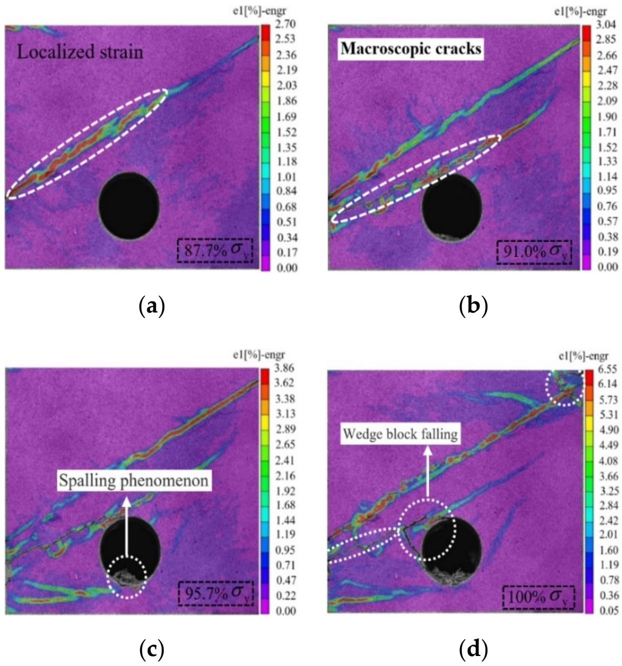

Figure 21. Evolution process of the major principal strain field of sample L-3. (**a**) 87.7%σ_y; (**b**) 91.0%σ_y; (**c**) 95.7%σ_y; (**d**) 100%σ_y.

The evolution process of the major principal strain field of control group O is shown in Figure 22. Figure 22 shows that when the load reached 87.30% of the peak strength, slender cracks along the vertical direction appeared at both the roof and floor of the hole, and an obvious high-stress concentration was observed at the fracture plane. When the load reached 89.36% of the peak strength, the granite sample was in a state of compression, and a floccule-like high-strain zone appeared on the right side of the footwall. When the load reached 93.28% of the strength, the cracks generated from the roof and floor of the hole began to vanish gradually, and small-scale high strain began to appear at the right corner of the hanging wall. When the load reached 100% of the peak strength, the cracks initiated from the roof and floor of the hole closed completely, leaving only a belt crack derived from the oblique bottom of the hole. The high-strain concentration zone in the upper part of the fracture plane was enlarged and accompanied by the formation of several horizontal macrocracks, and the high-stress concentration also occurred in the left end of the fracture plane.

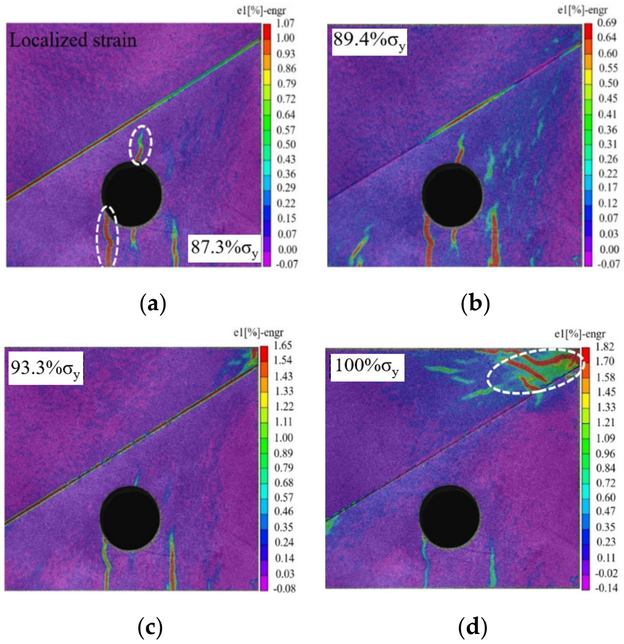

Figure 22. Evolution process of the major principal strain field of sample O. (**a**) 87.3%σ_y; (**b**) 89.4%σ_y; (**c**) 93.3%σ_y; (**d**) 100%σ_y.

For the failure process of the unbonded fracture O, the phenomenon that was different from other types of samples was that cracks were not generated near the fracture plane, and cracks still occurred around the hole. The failure of the sample was caused by the high-strain concentration at both ends of the fracture plane. The appearance of macroscopic cracks led to the fracturing and final failure of the granite material.

4.2.2. Displacement Field Characteristics

It was found that displacement nucleation existed in the vertical displacement field. More specifically, the vertical displacement between the fracture plane and the hole was nucleated, and the displacement value gradually decreased from the inside to the outside, as shown in Figure 23.

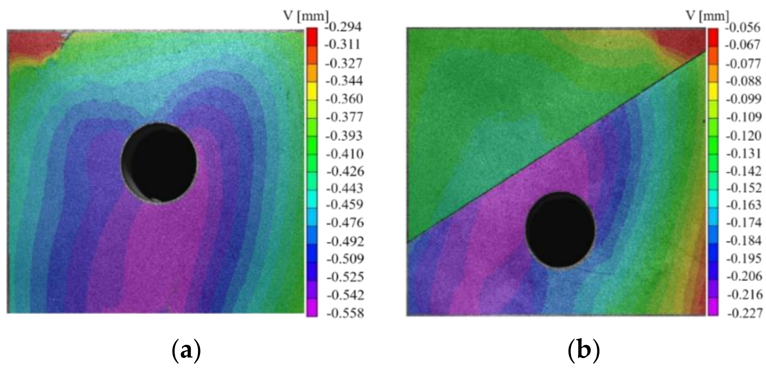

Figure 23. *Cont.*

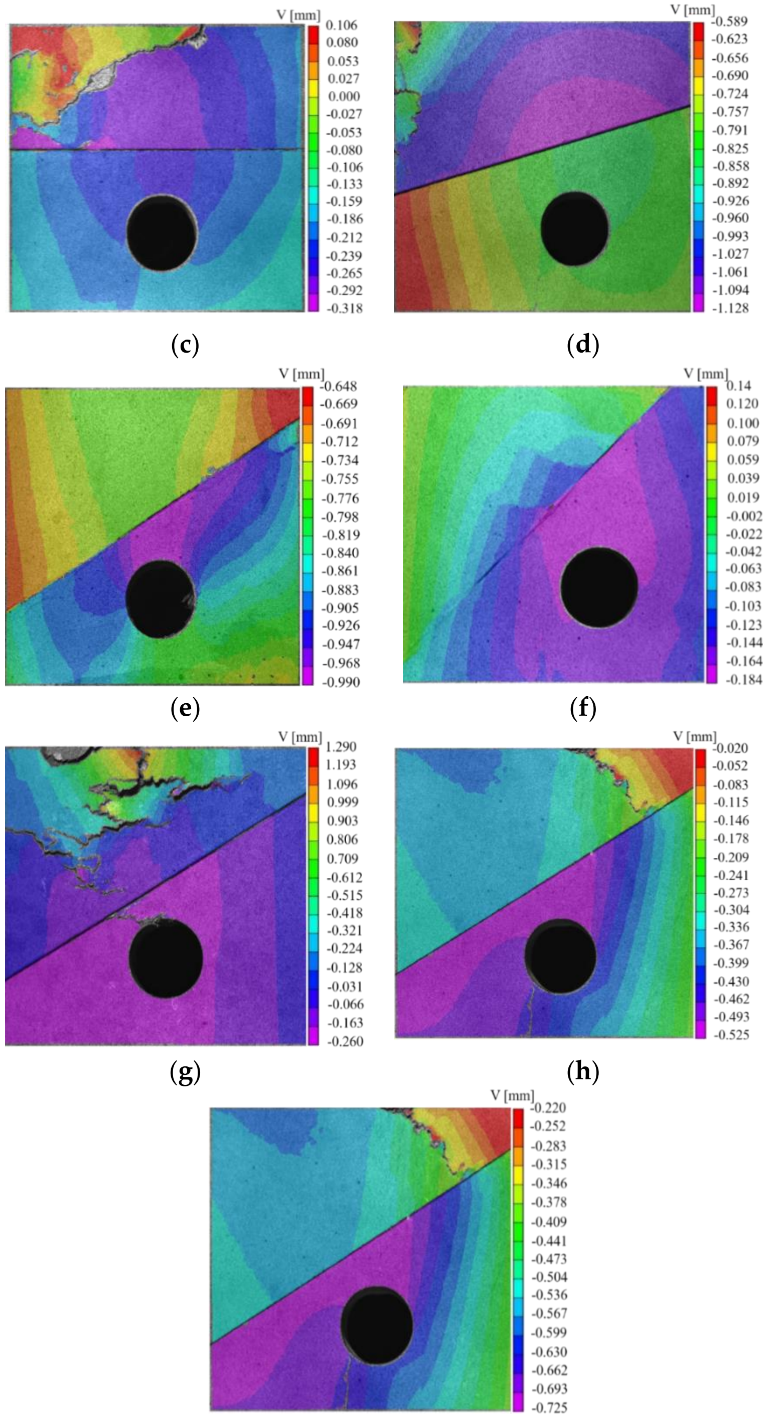

Figure 23. Nucleation phenomena of different types of granite samples; (**a**) Sample C (99.2%); (**b**) Sample O (97.5%); (**c**) Sample A-0 (96.2%); (**d**) Sample A-15 (99.3%); (**e**) Sample A-30 (94.6%); (**f**) Sample A-45 (96.6%); (**g**) Sample L-1 (99.8%); (**h**) Sample L-2 (98.9%); (**i**) Sample L-3 (98.3%).

The vertical displacement image of the granite sample with a hole is shown in Figure 23a. The phenomenon of displacement nucleation appeared below the hole, indicating that the microunits below the hole all moved downward. The vertical displacement images of granite samples with bonded fractures of 0°, 15° and 30°, 45°, and unbonded fractures are shown in Figure 23b–d. The red to purple in the legend indicates that the displacement value increased downward. Figure 23 shows that there was a purple nuclear displacement zone between the fracture and the hole, which meant that the vertical displacement of the micro units within the fracture-hole structure demonstrated a downward movement under loading. Nucleation occurred when the vertical displacements reached 0.318 mm, 1.128 mm, 0.990 mm, and 0.184 mm. In group A, nucleation was more difficult to occur when the angle of the fracture was 15° and was most likely to occur when the angle of the fracture was 45°.

Figure 23g–i show the vertical displacement images of granite samples *L*-1, *L*-2, and *L*-3, respectively. The nucleation types of rock samples were centered on the region between the fracture and hole. Extending toward the left region of the footwall rather than spreading out similar to the types in group A, the nucleation types of the granite samples occurred when the vertical displacement reached 0.260 mm, 0.525 mm, and 0.726 mm. This indicated that with the increase in the spacing distance *L*, the micro units needed to move downward further in the vertical direction to form the nucleation.

5. Conclusions

The main conclusions are summarized as follows:

(1) Failure mode: With the increase in fracture dip angle, the number of macroscopic cracks also increases, and the failure degree is more severe. When the spacing distance *L* decreases, the circular hole has a great influence on the fracture plane, and the newly formed cracks accumulate in the middle region and further spread upward across the fracture plane. Therefore, to avoid roadway engineering accidents, it is necessary to avoid faults with large dip angles and keep a long distance from the fault as far as possible during roadway construction

(2) Fracture slip: when the fracture dip angle changes from 0° to 30°, the slip value at the measurement points (point A is far from the loading platen, point B is located above the hole, and point C is near the loading platen) along the fracture demonstrates less correlation. When the fracture dip angle is 45°, the slip value at the ends of the fracture plane (points A, B) is quite small, and the slip value of point B above the hole is significantly higher than that of the fracture ends. When the fracture is close to the hole, the slip value above the hole (point B) is the largest, and the slip value at point A far from the loading position is the smallest. When the fracture is far from the hole, the influence of the hole on fracture slip is reduced.

(3) Discontinuity of displacement: the displacement drops between the hanging wall and footwall increase with increasing fracture dip angle for both horizontal and vertical displacement. Furthermore, the displacement drop in the vertical direction is relatively small and is almost 50% lower than that in the horizontal direction. The closer the spacing distance between the fracture and the hole is, the more obvious the discontinuity of displacement. The closer the hole is to the fracture, the more likely the sample will be destroyed and the more serious the damage degree will be.

(4) The major principal strain field reveals the initiation, propagation, and coalescence of crack processes for different types of granite samples, and the displacement nucleation phenomenon is observed in the vertical displacement field.

Author Contributions: Conceptualization, D.L.; methodology, D.L.; F.G., J.J.; software, F.G.; validation, J.J., F.G.; formal analysis, J.J.; funding acquisition, D.L. All authors have read and agreed to the published version of the manuscript.

Funding: National Natural Science Foundation of China (NSFC) 52074349.

Data Availability Statement: The data presented in this study are available on request from the corresponding author.

Conflicts of Interest: The authors declare no conflict of interest.

References

1. Bruneau, G.; Tyler, D.B.; Hadjigeorgiou, J.; Potvin, Y. Influence of faulting on a mine shaft—A case study: Part I—Background and instrumentation. *Interna-Tional J. Rock Mech. Min. Sci.* **2003**, *40*, 95–111. [CrossRef]
2. Kun, M.; Onargan, T. Influence of the fault zone in shallow tunneling: A case study of Izmir Metro Tunnel. *Tunn.-Ling Undergr. Space Technol. Inc. Trenchless Technol. Res.* **2013**, *33*, 34–45. [CrossRef]
3. Zhao, K.; Janutolo, M.; Barla, G.; Chen, G. 3D simulation of TBM excavation in brittle rock associated with fault zones: The Brenner Exploratory Tunnel case. *Eng. Geol.* **2014**, *181*, 93–111. [CrossRef]
4. Panthee, S.; Singh, P.K.; Kainthola, A.; Singh, T.N. Control of rock joint parameters on deformation of tunnel opening. *J. Rock Mech. Geotech. Eng.* **2016**, *8*, 489–498. [CrossRef]
5. O'Rourke, M.J.; Liu, X. *Seismic Design of Buried and Offshore Pipelines, Monograph Series*; Multidisciplinary Center for Earthquake Engineering Research, (MCEER): New York, NY, USA, 2012.
6. Liu, Z.X.; Liu, J.Q.; Pei, Q.; Yu, H.T.; Li, C.C.; Wu, C.Q. Seismic response of tunnel near fault fracture zone under incident SV waves. *Undergr. Space* **2021**, *6*, 695–708. [CrossRef]
7. Zhang, Z.Q.; Chen, F.F.; Li, N.; He, M.M. Influence of Fault on the Surrounding Rock Stability for a Mining Tunnel: Distance and Tectonic Stress. *Adv. Civ. Eng.* **2019**, *2019*, 2054938. [CrossRef]
8. Sabagh, M.; Ghalandarzadeh, A. Numerical modelings of continuous shallow tunnels subject to reverse faulting and its verification through a centrifuge. *Comput. Geotech.* **2020**, *128*, 103813. [CrossRef]
9. Zhong, Z.L.; Wang, Z.; Zhao, M.; Du, X.L. Structural damage assessment of mountain tunnels in fault fracture zone subjected to multiple strike-slip fault movement. *Tunn. Undergr. Space Technol.* **2020**, *104*, 103527. [CrossRef]
10. Chu, B.L.; Hsu, S.C.; Chang, Y.L.; Lin, Y.S. Mechanical behavior of a twin-tunnel in multi-layered formations. *Tunn. Undergr. Space Technol.* **2007**, *22*, 351–362. [CrossRef]
11. Li, D.; Gao, F.; Han, Z.; Zhu, Q. Experimental evaluation on rock failure mechanism with combined flaws in a connected geometry under coupled static-dynamic loads. *Soil Dyn. Earthq. Eng.* **2020**, *132*, 106088. [CrossRef]
12. Huang, F.; Wu, C.; Ni, P.; Wan, G.; Karekal, S. Experimental analysis of progressive failure behavior of rock tunnel with a fault zone using non-contact DIC technique. *Int. J. Rock Mech. Min. Sci.* **2020**, *132*, 104355. [CrossRef]
13. Li, D.; Meng, L.; Han, Z.; Zhou, Z. Dynamic compressive mechanical properties of bedding sandstone with pre-existing hole. *Meitan Xuebao/J. China Coal Soc.* **2019**, *44*, 1349–1358.
14. Wang, S.; Ni, P.; Guo, M. Spatial characterization of joint planes and stability analysis of tunnel blocks. *Tunn. Undergr. Space Technol. Inc. Trenchless Technol. Res.* **2013**, *38*, 357–367. [CrossRef]
15. Yang, S.; Liu, X.; Li, Y. Experimental analysis of mechanical behavior of sandstone containing hole and fissure under uniaxial compression. *Chin. J. Rock Mech. Eng.* **2012**, *31*, 3539–3546.
16. Zhou, Y.; Zhu, Q.; Diyuan, L.I.; Chunde, M.A. Experimental study on mechanical and failure characteristics of sandstone with a filled elliptical hole. *J. Railw. Sci. Eng.* **2019**, *142*, 106780.
17. Li, D.Y.; Zhu, Q.Q.; Zhou, Z.L.; Li, X.B.; Ranjith, P.G. Fracture analysis of marble specimens with a hole under uniaxial compression by digital image correlation. *Eng. Fract. Mech.* **2017**, *183*, 109–124. [CrossRef]
18. Liu, J.P.; Li, Y.H.; Xu, S.D.; Xu, S.; Jin, C.Y.; Liu, Z.S. Moment tensor analysis of acoustic emission for cracking mechanisms in rock with a pre-cut circular hole under uniaxial compression. *Eng. Fract. Mech.* **2015**, *135*, 206–218. [CrossRef]
19. Pan, P.; Ding, W.; Feng, X.; Yao, H.; Zhou, H. Research on influence of pre-existing crack geometrical and material properties on crack propagation in rocks. *Chin. J. Rock Mech. Eng.* **2008**, *27*, 1882–1889.
20. Zhu, T.T.; Jing, H.W.; Su, H.J.; Yin, Q. Experimental investigation on mechanical behavior of sandstone with coupling effects under uniaxial compression. *Meitan Xuebao/J. China Coal Soc.* **2015**, *40*, 1518–1525.
21. Li, Y.; Liu, J.; Tang, X.; Yang, S.; Liu, D. Simulation analysis of mechanical properties of the soft rock mass with holes and fractures. *J. Min. Saf. Eng.* **2020**, *37*, 594–603.
22. Yin, Q.; Jing, H.W.; Su, H.J. Investigation on mechanical behavior and crack coalescence of sandstone specimens containing fissure-hole combined flaws under uniaxial compression. *Geosci. J.* **2018**, *22*, 825–842. [CrossRef]
23. Feng, F.; Li, X.; Li, D.; Chong, C. Numerical analysis of failure characteristics of circular hole specimen containing pre-existing flaw based on finite/discrete element method. *Yantu Lixue/Rock Soil Mech.* **2017**, *38*, 337–348.
24. Geng, P.; Yue, H.E.; Chuan, H.E.; Quan, Q.; Yan, Q. Research on reasonable aseismic fortified length for tunnel through fault fracture zone. *Chin. J. Rock Mech. Eng.* **2014**, *33*, 358–365.
25. Gu, Y.; Li, W.; Li, H. Experimental study on the relative distance between a tunnel and a fault and subsequent effects on the stability of the surrounding rock. *Mod. Tunn. Technol.* **2013**, *50*, 59–65.
26. Geng, P.; Chuan, W.U.; Tang, J.; Lin, L.I. Analysis of dynamic response properties for tunnel through fault fracture zone. *Chin. J. Rock Mech. Eng.* **2012**, *31*, 1406–1413.
27. Jiang, J.P.; Zhang, Y.S. Study on the influence of dip angles of normal fault on tunnel surrounding rocks in the fault footwall. *Caikuang Yu Anquan Gongcheng Xuebao/J. Min. Saf. Eng.* **2011**, *28*, 596–601.
28. Jiao, P.; Lai, H. Theoretical analysis on the influence of different dip angle reverse faults' dislocation on tunnel structure. *China Civ. Eng. J.* **2019**, *52*, 106–117.
29. Dalgic, S. Tunneling in fault zones, Tuzla tunnel, Turkey. *Tunn. Undergr. Space Technol.* **2003**, *18*, 453–465. [CrossRef]

30. Mohammadi, H.; Azad, A. Prediction of ground settlement and the corresponding risk induced by tunneling: An application of rock engineering system paradigm. *Tunn. Undergr. Space Technol.* **2021**, *110*, 103828. [CrossRef]
31. Han, Z.Y.; Li, D.Y.; Zhou, T.; Zhu, Q.Q.; Ranjith, P.G. Experimental study of stress wave propagation and energy characteristics across rock specimens containing cemented mortar joint with various thicknesses. *Int. J. Rock Mech. Min. Sci.* **2020**, *131*, 104352. [CrossRef]
32. Xiao, P.; Li, D.Y.; Zhao, G.Y.; Liu, M. Experimental and Numerical Analysis of Mode I Fracture Process of Rock by Semi-Circular Bend Specimen. *Mathematics* **2021**, *9*, 1769. [CrossRef]
33. Xiao, P.; Li, D.Y.; Zhu, Q.Q. Strain Energy Release and Deep Rock Failure Due to Excavation in Pre-Stressed Rock. *Minerals* **2022**, *12*, 488. [CrossRef]
34. Li, D.Y.; Zhang, C.X.; Zhu, Q.Q.; Ma, J.Y.; Gao, F.H. Deformation and fracture behavior of granite by the short core in compression method with 3D digital image correlation. *Fatigue Fract. Eng. Mater. Struct.* **2022**, *45*, 425–440. [CrossRef]
35. Li, D.Y.; Ma, J.Y.; Wan, Q.R.; Zhu, Q.Q.; Han, Z.Y. Effect of thermal treatment on the fracture toughness and subcritical crack growth of granite in double-torsion test. *Eng. Fract. Mech.* **2021**, *253*, 107903. [CrossRef]
36. Kun, D.U.; Li, X.B.; Li, D.Y.; Weng, L. Failure properties of rocks in true triaxial unloading compressive test. *Trans. Nonferrous Met. Soc. China* **2015**, *25*, 571–581.
37. Li, X.B.; Du, K.; Li, D.Y. True Triaxial Strength and Failure Modes of Cubic Rock Specimens with Unloading the Minor Principal Stress. *Rock Mech. Rock Eng.* **2015**, *48*, 2185–2196. [CrossRef]
38. Chen, J.; Feng, X. True triaxial experimental study on rock with high geostress. *Yanshilixue Yu Gongcheng Xuebao/Chin. J. Rock Mech. Eng.* **2006**, *25*, 1537–1543.
39. Han, Z.; Li, D.; Li, X. Dynamic mechanical properties and wave propagation of composite rock-mortar specimens based on SHPB tests. *Int. J. Min. Sci. Technol.* **2022**, *32*, 793–806. [CrossRef]
40. Gong, F.; Luo, Y.; Si, X.; Li, X. Experimental modelling on rockburst in deep hard rock circular tunnels. *Chin. J. Rock Mech. Eng.* **2017**, *36*, 1634–1648.
41. Han, Z.; Li, D.; Li, X. Effects of axial pre-force and loading rate on Mode I fracture behavior of granite. *Int. J. Rock Mech. Min. Sci.* **2022**, *157*, 105172. [CrossRef]